



The synergistic effect of graphitic N and pyrrolic N for the enhanced photocatalytic performance of nitrogen-doped graphene/TiO₂ nanocomposites



Ying Xu^a, Yanping Mo^a, Jing Tian^a, Ping Wang^a, Huogen Yu^{a,b,*}, Jiaguo Yu^c

^a School of Chemistry, Chemical Engineering and Life Sciences, Wuhan University of Technology, Wuhan 430070, PR China

^b State Key Laboratory of Silicate Materials for Architectures, Wuhan University of Technology, Wuhan 430070, PR China

^c State Key Laboratory of Advanced Technology for Material Synthesis and Processing, Wuhan University of Technology, Wuhan 430070, PR China

ARTICLE INFO

Article history:

Received 22 June 2015

Received in revised form 26 August 2015

Accepted 30 August 2015

Available online 2 September 2015

Keywords:

Synergistic effect

N-doped graphene

Electron mediator

Reduction active site

ABSTRACT

The functionalization of graphene by nitrogen doping is an excellent method to modify the photocatalytic performance of graphene-based photocatalysts. However, the effect of N-bonding configurations (such as pyrrolic N, pyridinic N and graphitic N) on the photocatalytic performance of nitrogen-doped graphene/TiO₂ composite (N-rGO/TiO₂) has seldom been investigated. In this study, the different nitrogen sources (NH₃, N₂H₄, and CO(NH₂)₂) have been used to prepare the N-rGO/TiO₂ with the aim of obtaining different N-bonding configurations in graphene. It was found that when the NH₃ and CO(NH₂)₂ were used as the N-doping precursors, the resultant N-rGO/TiO₂ photocatalysts mainly showed the pyrrolic N (>70%) and pyridinic N (>10%). As for the N₂H₄ precursor, the prepared N-rGO/TiO₂(N₂H₄) primarily exhibited the pyrrolic N (ca. 63%) and graphitic N (ca. 37%) in graphene. The photocatalytic results indicated that all the N-rGO/TiO₂ showed an obviously enhanced photocatalytic performance compared with the undoped rGO/TiO₂. Moreover, the N-rGO/TiO₂(N₂H₄) displayed the highest photocatalytic activity ($k = 0.29 \text{ min}^{-1}$), which is remarkably larger than that of TiO₂ and rGO/TiO₂ by a factor of 3.63 and 2.64, respectively. On the basis of the above results, a synergistic effect of graphitic N and pyrrolic N in graphene is proposed to account for the enhanced photocatalytic performance of N-rGO/TiO₂(N₂H₄), namely, the graphitic-N doped graphene serves as an effective electron-transfer mediator for the photo-generated electrons while the pyrrolic-N doped graphene functions as the oxygen-reduction active site to rapidly promote the following interfacial catalytic reaction. It is quite believed that the synthetic effect of electron-transfer mediator and oxygen reduction activation site is a general and effective strategy for the design of high-performance photocatalytic materials.

© 2015 Elsevier B.V. All rights reserved.

1. Introduction

Photocatalysis is one of the effective strategies to solve the energy and environmental problems [1–3]. TiO₂ semiconductor, the most promising and versatile material, has attracted intense attention due to its outstanding physical and chemical stability, inexpensiveness, non-toxicity, and appropriate electronic band structure. Nevertheless, the currently available TiO₂ photocatalysts generally suffer from a low photocatalytic efficiency, which

significantly has a great effect on the practical applications. To modify the photocatalytic activity of TiO₂, various methods such as doping various ions into the TiO₂ lattice [4], sensitization via absorbed molecules [5–7], coupling with low band-gap materials [8,9], and the surface loading by various cocatalysts [10–13], have been widely designed and developed. Among them, the cocatalyst loading on the photocatalyst surface has been found to be one of the most effective and facile strategies for the enhancement of TiO₂ photocatalytic materials. Considering the expensive cost of the well-known noble metal cocatalysts (such as, Pt, Au, Pd) [14,15], it is highly required to develop highly efficient and low-cost cocatalysts for the modification of TiO₂ with the aim of improving its photocatalytic activity.

Graphene, a two-dimensional monolayer material form of sp²-bonded carbon atoms, has been demonstrated to be an excellent

* Corresponding author at: School of Chemistry, Chemical Engineering and Life Sciences, Wuhan University of Technology, Wuhan 430070, PR China. Fax: +86 27 87879468.

E-mail address: yuhuogen@whut.edu.cn (H. Yu).

support as well as an electron cocatalyst owing to its large specific surface area and high electron mobility [16–18]. In the past several years, the graphene has been introduced in the photocatalytic field and was found to be an effective electron-cocatalyst to improve the photocatalytic performance of TiO_2 [19–25]. In recent years, we have also developed several methods to prepare various graphene-based photocatalysts with enhanced photocatalytic performance [26–29]. In addition to the naked graphene-based composite materials, the functionalization of graphene (such as, chemical doping and surface modification) has also been widely investigated and applied in photocatalysis [30]. Recently, the nitrogen doping into the graphene nanosheets was found to be an effective strategy to greatly improve the photocatalytic performance of photocatalysts [31–33]. Pei et al. [34] reported that the photocatalytic hydrogen evolution of N- TiO_2 could be effectively improved by N-graphene. Mou et al. [31] also found that the N-graphene/ TiO_2 nanocomposites showed a higher photocatalytic activity for hydrogen production than the TiO_2 and rGO/ TiO_2 due to the higher electrical conductivity of N-graphene. In addition, many other researchers also demonstrated that various photocatalysts such as AgBr [32,35], MoS_2 [36], ZnSe [37], and CdS [38] showed a higher photocatalytic performance by grafting N-graphene. However, it is well known that the physical–chemical properties of graphene (e.g. electron mobility) can be greatly affected by the microstructure change of functionalized graphene. In fact, three typical N-bonding configurations such as graphitic N (or quaternary N), pyridinic N, and pyrrolic N, have been widely reported and usually can be formed in the graphene nanosheets by doping N element [30]. However, the above reported results about the N-graphene are mainly restricted to their synthesis and corresponding enhanced photocatalytic performance, and seldom investigations have been focused on the effect of different N-bonding configuration on the photocatalytic performance of N-graphene based photocatalysts.

In this study, we try to prepare the N-doped graphene with different N-bonding configurations, and investigate the effect of N-bonding configuration on the microstructures and photocatalytic performance of photocatalyst. The commercial P25 TiO_2 nanoparticle is used as the typical photocatalyst source. The nanocomposite of N-doped reduced graphene oxide and TiO_2 nanoparticle (N-rGO/ TiO_2) was prepared by a facile hydrothermal method via the addition of different nitrogen sources. The morphology and microstructures of N-rGO/ TiO_2 were carefully characterized by various technologies. A possibly mechanism about the N-doped graphene as an effective electron cocatalyst was proposed to account for the enhanced photocatalytic performance of N-rGO/ TiO_2 . To the best of our knowledge, this is the first report about the effect of N-bonding configuration on the photocatalytic performance of N-rGO/ TiO_2 composites. This work may provide new insight for smart design and synthesis of other N-doped graphene based composites with special functions.

2. Experimental

Graphene oxide (GO) was synthesized from natural graphite powder (99.95%) according to a modified Hummers method, and the GO solution (1 mg/mL) was obtained by ultrasonic dispersion of GO powder in distilled water for 2 h [26,27]. Commercial P25 was calcined at 550°C in order to obtain a clean TiO_2 surface, which is suitable for the following preparation of rGO- TiO_2 nanocomposite with a strongly coupling interface [26]. Unless otherwise specified, all the other chemicals are analytical grade supplied by Shanghai Chemical Reagent Ltd. (PR China) and used as received without further purification.

2.1. Synthesis of N-rGO/ TiO_2 photocatalyst

N-rGO/ TiO_2 photocatalyst were prepared by a simple hydrothermal method with the addition of different nitrogen sources (such as NH_3 , N_2H_4 , and $\text{CO}(\text{NH}_2)_2$) for the N doping. In our previous studies, it was found that when the GO amount ($W_{\text{GO}}/W_{\text{TiO}_2}$) was controlled to be 1 wt%, the resulting rGO/ TiO_2 showed the highest photocatalytic activity [26]. Therefore, in this study, the amount of GO in all the N-rGO/ TiO_2 samples was controlled to be 1 wt%.

For a typical synthesis, 0.2 g of TiO_2 nanoparticles was dispersed into 8 mL of deionized water, and then 2 mL of GO solution was added into the above suspended solution. Owing to the well coupling interface between the calcined TiO_2 nanoparticles and GO nanosheets, a homogeneous GO- TiO_2 suspended solution can be easily obtained. After stirring for 30 min, the corresponding amount of nitrogen source was added into the GO- TiO_2 suspended solution. After stirring for another 3 h, the mixed solution was transferred into a Teflon-lined stainless steel autoclave and heated at 200°C for 12 h. The resultant N-rGO/ TiO_2 composites were recovered by filtration, washing and dried at 70°C . To investigate the effect of nitrogen amount on the photocatalytic performance of N-rGO/ TiO_2 composites, the amount of N element in N sources ($W_{\text{N}}/W_{\text{GO}}$) were controlled to be 0, 0.5, 1, 3, 5, and 10 wt%. According to the photocatalytic results, it was found that the 5 wt% of N-rGO/ TiO_2 showed the highest photocatalytic activity. To investigate the effect of different N sources on the microstructures and photocatalytic performance, in this study, the 5 wt% of N-rGO/ TiO_2 photocatalysts are prepared from NH_3 , N_2H_4 , and $\text{CO}(\text{NH}_2)_2$, and the corresponding samples were referred to be N-rGO/ TiO_2 (NH_3), N-rGO/ TiO_2 (N_2H_4) and N-rGO/ TiO_2 ($\text{CO}(\text{NH}_2)_2$), respectively.

For the preparation of Cu(II)- or Fe(III)-modified N-rGO/ TiO_2 (N_2H_4) photocatalysts, a typical impregnation method, which has been widely reported in our previous results [11,39], has been applied, and the amount of Cu(II) or Fe(III) was controlled to be 0.2 wt% ($M/\text{TiO}_2 = 0.2 \text{ wt\%}$, $M = \text{Cu(II)}$ or Fe(III)).

2.2. Characterization

X-ray diffraction (XRD) patterns were obtained on a D/MAX-RBX-ray diffractometer (Rigaku, Japan). Morphological images were obtained on a Quanta $\times 50$ field emission scanning electron microscope (FESEM) (USA-FEI) and JEM-2100F transmission electron microscopy (TEM, JEOL, Japan). X-ray photoelectron spectroscopy (XPS) measurements were done on a KRATOA XSAM800 XPS system with Mg $K\alpha$ source. Raman spectra were collected using an INVIA spectrophotometer (Renishaw, UK). Fourier Transform Infrared spectra (FTIR) were acquired using a Nexus FT-IR spectrophotometer (Thermo Nicolet, America). UV–vis absorption spectra were obtained using a UV–visible spectrophotometer (UV-2550, SHI-MADZU, Japan).

2.3. Photocatalytic activity

The evaluation of photocatalytic activity of the prepared samples for the decomposition of methyl orange (MO) and phenol aqueous solution was performed at room temperature. Experimental steps were shown as follows: 50 mg of the sample was dispersed into 10 mL of MO solution (20 mg L^{-1}) or phenol solution (10 mg/L) in a disk with a diameter of ca. 5 cm. The mixed suspension reached an adsorption–desorption equilibrium in dark for 1 h under room conditions. The disk was exposed to 350 W Xe lamp with a UV cutoff filter ($\lambda > 400 \text{ nm}$). At certain time intervals, the concentration of MO (or phenol) solution was measured by an UV–visible spectrophotometer (UV-1240, SHIMADZU, Japan). For the low-concentration MO solution, its photocatalytic kinetics can

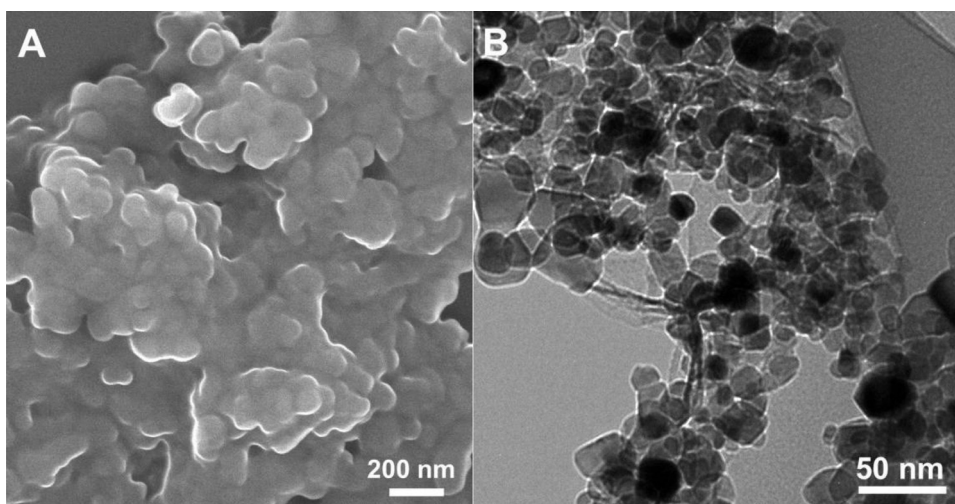


Fig. 1. Typical FESEM (A) and TEM (B) images of N-rGO/TiO₂(N₂H₄).

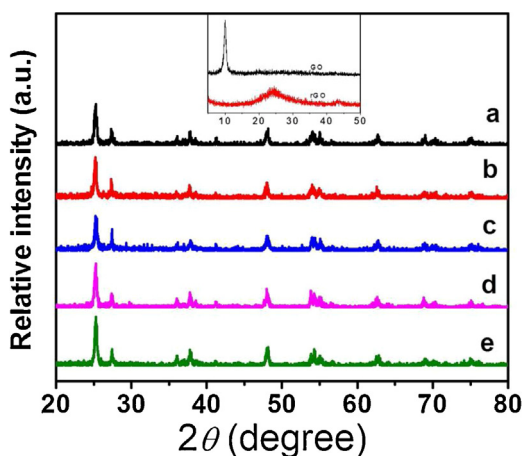


Fig. 2. XRD patterns of various samples: (a) TiO₂; (b) rGO/TiO₂; (c) N-rGO/TiO₂(NH₃); (d) N-rGO/TiO₂(N₂H₄); and (e) N-rGO/TiO₂(CO(NH₂)₂); inset showing the XRD patterns of GO and rGO obtained from hydrothermal method.

be expressed as $\ln(c/c_0) = -kt$ (a pseudo-first-order reaction), where k is the rate constant, and c_0 and c are the initial MO (or phenol) concentration and the t -min irradiated MO (or phenol) concentration, respectively.

3. Results and discussion

3.1. Microstructures of N-rGO/TiO₂

It is well-known that commercial P25 TiO₂ nanoparticles can be well dispersed in water to form a homogeneous suspended solution. To further improve their coupling interaction with the GO nanosheets that showing an excellent hydrophilic property, P25 TiO₂ was calcined at 550 °C for 0.5 h in order to obtain a clean and hydrophilic surface [26]. Therefore, the well coupling interface between the TiO₂ particles and the rGO nanosheets can be clearly found in the FESEM and TEM images in our previous study [26]. After the N doping into rGO, the resultant N-rGO/TiO₂ shows a similar morphology and structure due to a very limited N amount (N/rGO = 5 wt%; rGO/TiO₂ = 1 wt%) (Fig. 1). Fig. 2 shows the XRD patterns of the N-rGO/TiO₂ samples prepared from various N sources. All the resultant N-rGO/TiO₂ samples show a similar diffraction peaks as the pure TiO₂, suggesting that the phase structure and crystallization of TiO₂ cannot be effected by the addition of N-rGO

Table 1

Peak area ratios of various N-binding configurations to total area (obtained by XPS).

Samples	$A_{(\text{pyridinicN})}/A$	$A_{(\text{pyrrolicN})}/A$	$A_{(\text{graphiticN})}/A$
N-rGO(NH ₃)	0.15	0.77	0.08
N-rGO(N ₂ H ₄)	0.00	0.63	0.37
N-rGO(CO(NH ₂) ₂)	0.17	0.74	0.09

due to a very limited amount (1 wt%). However, after hydrothermal treatment, it is clear that the GO nanosheets can be effectively reduced to form rGO (inset in Fig. 2), in good agreement with the reported results [40,41].

After hydrothermal reaction of GO in different N sources (NH₃, N₂H₄, and CO(NH₂)₂), the chemical states of N in the hexagonal lattice of graphene were significantly changed, which can be well illustrated by the XPS results (Fig. 3 and Table 1). Usually, three typical N-binding configurations such as pyrrolic N, pyridinic N, and graphitic N, can be found in the N-doped graphene (Fig. 3A) [30,42]. The pyrrolic N is caused by the incorporation of N atoms into a five-membered heterocyclic ring, and pyridinic N is from the sp² hybridized N atom with two sp² hybridized C neighbors, while the graphitic N comes from sp² hybridized N atoms with three sp² hybridized C. Fig. 3B shows the N 1s XPS spectra of N-rGO samples obtained from different N sources. It is found that the N-rGO samples obviously show the different N-binding configurations for different N sources. When the NH₃ and CO(NH₂)₂ were used as the N sources for doping, the XPS spectra of N 1s can be decomposed into three typical peaks, which corresponds to the pyridinic N (ca. 398.2 eV), pyrrolic N (ca. 399.8 eV) and graphitic N (401.9 eV). However, when the N₂H₄ was introduced into the graphene, the XPS spectra of N 1s can be mainly ascribed to the pyrrolic N and graphitic N. To further investigate the relative amount of various N-binding, the peak area ratios of the various N-binding configurations to total area are calculated and the corresponding results are shown in Table 1. It is clear that the pyrrolic N is the main N-binding configuration for all the N-doped graphene samples although different N sources are used as the precursors, which is in good agreement with the Xu's report about the pyrrolic N-doped graphene prepared by a hydrothermal method [42]. In fact, the above result can be well explained by considering that the carbons on the graphene edges can be more easily replaced by N element due to their high reaction activity compared with the inner faultless sp²-bonded carbon atoms (such as the graphitic N). Further observation indicates that both of the N-rGO(NH₃) and N-rGO(CO(NH₂)₂) samples show a comparable composition for the various N bonding, and the pyrrolic

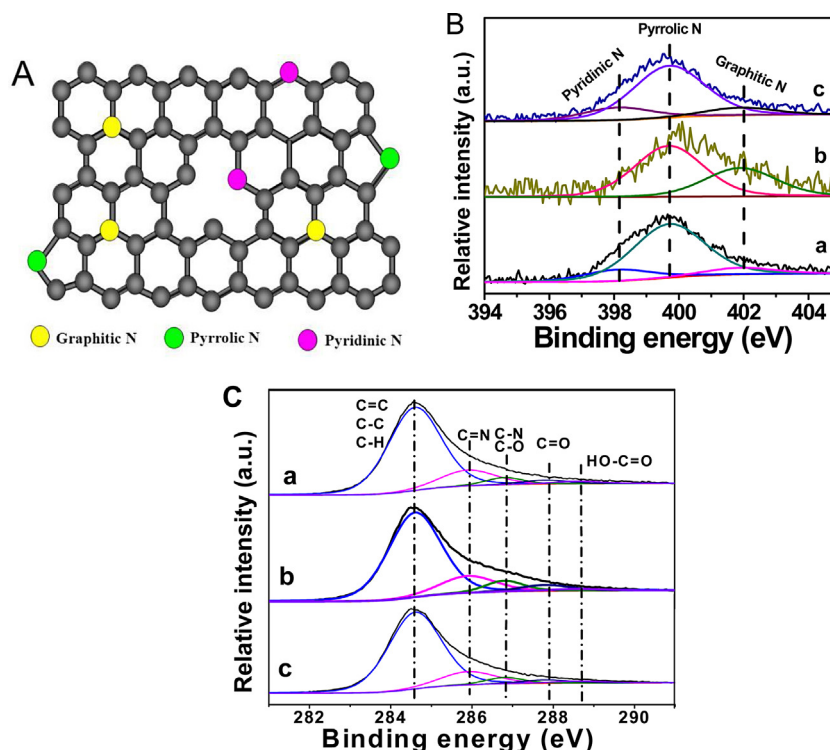


Fig. 3. (A) The three N-binding configurations for the N-doped graphene; (B and C) XPS spectra of N1s (B) and C1s (C) of the (a) N-rGO/TiO₂(NH₃), (b) N-rGO/TiO₂(N₂H₄), and (c) N-rGO/TiO₂(CO(NH₂)₂).

Table 2

Peak area ratios of various C-containing bonds to total area (according to XPS results).

Samples	A_{CC}/A	A_{CN}/A	A_{CO}/A	$A_{C=O}/A$	A_{COOH}/A
GO	0.50	0	0.38	0.10	0.2
rGO	0.87	0	0.09	0.01	0.03
N-rGO(NH ₃)	0.67	0.13	0.09	0.07	0.04
N-rGO(CO(NH ₂) ₂)	0.69	0.13	0.08	0.06	0.04
N-rGO(N ₂ H ₄)	0.66	0.12	0.11	0.08	0.03

N and pyridinic N are the main N-binding configurations (>90%) (Table 1). When the N₂H₄ was used to prepare the N-rGO(N₂H₄), it is interesting to observe that only pyrrolic N and graphitic N can be formed. Moreover, in addition to the main pyrrolic N (63 at%) with a slight decrease, one of the important changes is that the amount of graphitic N (37 at%) has an obvious increase, suggesting that the N₂H₄ can promote the formation of graphitic N in graphene. As for the C 1s XPS spectra (Fig. 3C, Fig. S1 and Table 2), all the samples show a similar curve and components, suggesting that the N precursor has no obvious effect on the chemical states of carbon atoms in graphene. In addition, the amount of C=N in all the N-rGO samples shows a comparable component (ca. 12 at%), and some oxygen-containing groups are still remained on the graphene surface due to the uncompleted deoxygenation reaction, in agreement with the previous results [26].

The FTIR and Raman spectra can provide further information for the effective formation of N-rGO/TiO₂ nanocomposite. Fig. 4 shows the FTIR spectra of various samples. Compared with the GO (Fig. 4a), various oxygen-containing groups (800–1900 cm⁻¹) in rGO (Fig. 4b) has a significant decrease, suggesting that the hydrothermal treatment is an effective method for the reduction of GO to rGO. In fact, considering a weak absorption peaks in the range of 800–1900 cm⁻¹ (Fig. 4b), the oxygen-containing groups cannot be completely removed by the hydrothermal method, in good agreement with the XPS results (Fig. 3C). The small amount of oxygen-containing groups on graphene can be well

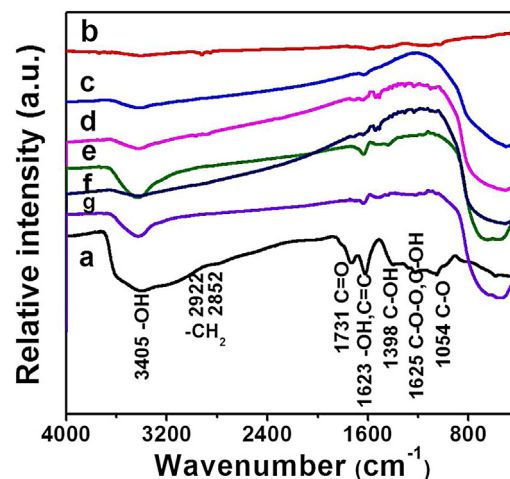


Fig. 4. FTIR spectra of various samples: (a) GO; (b) rGO; (c) TiO₂; (d) rGO/TiO₂; (e) N-rGO/TiO₂(NH₃); (f) N-rGO/TiO₂(N₂H₄); and (g) N-rGO/TiO₂(CO(NH₂)₂).

remained in all the rGO/TiO₂ (Fig. 4d) and N-rGO/TiO₂ (Fig. 4e–g) samples, suggesting that the surface microstructures of rGO is not greatly affected by the addition of various N sources. However, further observation indicates that the different nitrogen sources (NH₃, N₂H₄, and CO(NH₂)₂) have an obvious impact on the amount of oxygen-containing groups. The N-rGO/TiO₂(NH₃) and N-rGO/TiO₂(CO(NH₂)₂) show a comparable absorption-peak intensity, while the N-rGO/TiO₂(N₂H₄) clearly exhibits a decreased peak intensity for the oxygen-containing groups (3405, 1623, and 1398 cm⁻¹). The possible reasons are that in addition to the N-doping precursor similar to the NH₃ and CO(NH₂)₂, the N₂H₄ is a well-known reductant, which can cause the further reduction of GO during hydrothermal progress. Fig. 5 presents the Raman spectra of various samples. For TiO₂ sample (Fig. 5c), four strong

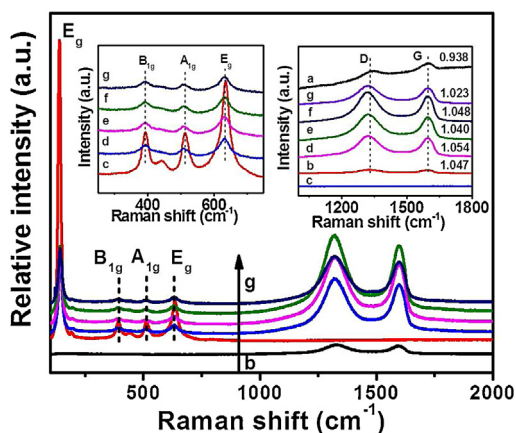


Fig. 5. Raman spectra of various samples: (a) GO; (b) rGO; (c) TiO₂; (d) rGO/TiO₂; (e) N-rGO/TiO₂(NH₃); (f) N-rGO/TiO₂(N₂H₄); and (g) N-rGO/TiO₂(CO(NH₂)₂).

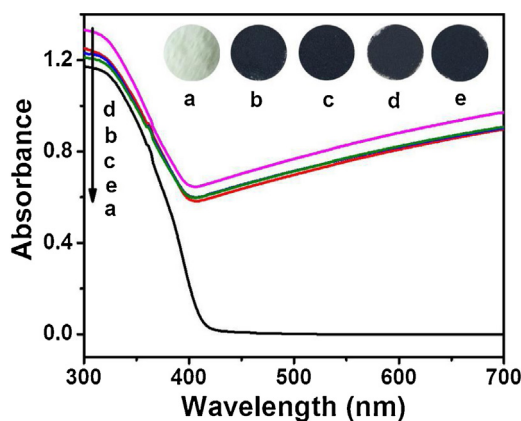


Fig. 6. UV-vis spectra and the corresponding photographs (inset) of various samples: (a) TiO₂; (b) rGO/TiO₂; (c) N-rGO/TiO₂(NH₃); (d) N-rGO/TiO₂(N₂H₄); and (e) N-rGO/TiO₂(CO(NH₂)₂).

characteristic peaks at 146 cm⁻¹ ($E_{g(1)}$), 397 cm⁻¹ (B_{1g}), 517 cm⁻¹ (A_{1g}), and 636 cm⁻¹ ($E_{g(2)}$) can be clearly observed [43]. However, it was found that all the characteristic peaks of TiO₂ exhibited a rapidly decreased intensity after the loading of rGO or N-rGO nanosheets (left inset in Fig. 5), which can be attributed to the excellent overlap of TiO₂ nanoparticles by the rGO or N-rGO nanosheets, as shown in the FESEM image (Fig. 1). In addition, it is well-known that the disorder or defects of N-rGO nanosheets can be evaluated by the relative intensity ratio of the D band to G band (I_D/I_G), and that a smaller value of the intensity ratio (I_D/I_G) is caused by the less sp³ defects/disorders in graphene nanosheets [44,45]. In this case, all the resultant N-rGO/TiO₂ prepared from the different N sources shows a comparable value of I_D/I_G with the rGO/TiO₂, which suggests that the N sources has no obvious effect on the disorder/defects of rGO nanosheets.

The effect of different N sources on the photoabsorption ability of the N-rGO/TiO₂ was investigated by UV-vis spectra (Fig. 6). For the pure TiO₂ sample, a typical band-gap absorption can be observed at ca. 400 nm. After loading with rGO, the resultant rGO/TiO₂ (Fig. 6b) shows improved visible-light absorption in the range of 400–700 nm. Considering the unchanged morphology and phase structure of TiO₂, the improved visible-light absorption of rGO/TiO₂ can only contributed to the black rGO nanosheets. In addition, after N doping into the graphene by various N sources, the resulting N-rGO/TiO₂ samples show similar absorption curves as the rGO/TiO₂, which is in agreement with their color (inset of Fig. 6).

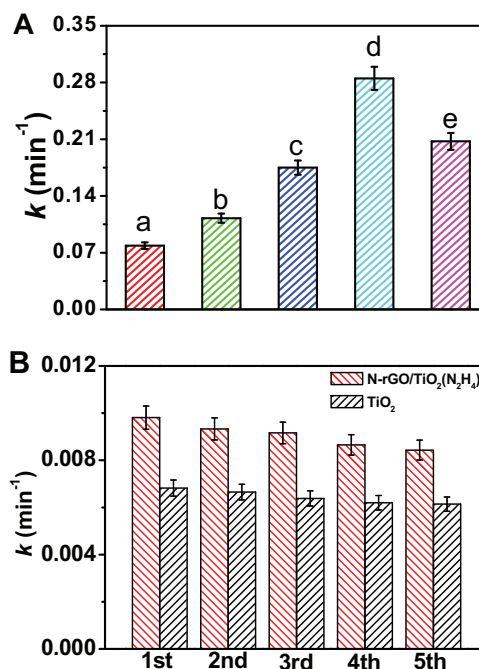


Fig. 7. (A) The photocatalytic degradation rate constant of MO for various photocatalysts: (a) TiO₂; (b) rGO/TiO₂; (c) N-rGO/TiO₂(NH₃); (d) N-rGO/TiO₂(N₂H₄); and (e) N-rGO/TiO₂(CO(NH₂)₂). (B) The repeated photocatalytic decomposition of phenol solution for the TiO₂ and N-rGO/TiO₂(N₂H₄) photocatalysts.

3.2. Photocatalytic performance

The photocatalytic performance of N-rGO/TiO₂ samples was first evaluated by the photocatalytic decolorization of MO aqueous solution. Firstly, the effect of nitrogen-source amount on the photocatalytic performance of N-rGO/TiO₂ composites was investigated, and it was found that when the amount of N source (N₂H₄) was ca. 5 wt% (N/rGO = 5 wt%), the resulting N-rGO/TiO₂ photocatalyst showed the highest photocatalytic activity (Fig. S2). With the addition of different N sources into the rGO nanosheets, the N-rGO/TiO₂ photocatalysts exhibited a completely different performance, as shown in Fig. 7A. It is clear that the pure TiO₂ (Fig. 7A(a)) shows an obvious photocatalytic activity and its apparent rate constant (k) is ca. 0.08 min⁻¹ owing to its well-known photocatalytic performance. When 1 wt% of rGO nanosheets were loaded on the TiO₂ surface, the resultant rGO/TiO₂ exhibited an clearly enhanced photocatalytic performance with a k value of 0.11 min⁻¹ (Fig. 7A(b)). The main reasons have been widely investigated and can be contributed to the rapid separation of photogenerated electrons and holes by the rGO nanosheet as an effective electron-cocatalyst. After the N element was introduced into the rGO nanosheets, the photocatalytic activity of N-rGO/TiO₂ samples can be further improved greatly, and the corresponding k values are 0.18 min⁻¹ for N-rGO/TiO₂(NH₃) (Fig. 7A(c)), 0.29 min⁻¹ for N-rGO/TiO₂(N₂H₄) (Fig. 7A(d)), and 0.21 min⁻¹ for N-rGO/TiO₂(CO(NH₂)₂) (Fig. 7A(e)). Obviously, the N-rGO/TiO₂(N₂H₄) showed the highest photocatalytic performance, and its rate constant (k) is remarkably larger than that of TiO₂ and rGO/TiO₂ by a factor of 3.63 and 2.64, respectively. To further investigate the photocatalytic decomposition ability and performance stability of the N-rGO/TiO₂(N₂H₄), the colorless phenol solution was also tested under an identical condition and the corresponding results were also shown in Fig. 7B. It was found that both pure TiO₂ and N-rGO/TiO₂ show a slightly decreased performance during repeating tests. However, compared with the pure TiO₂ photocatalyst, the N-rGO/TiO₂ also showed an obviously higher photocatalytic activity, suggesting the effective

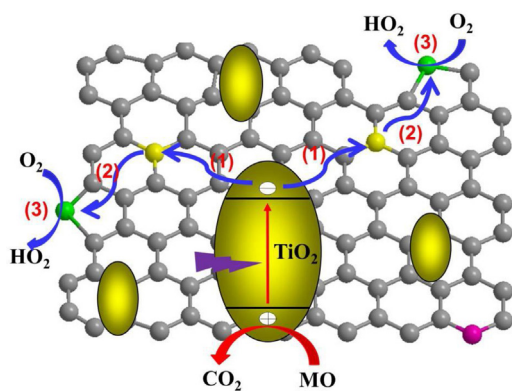


Fig. 8. The synergistic effect of graphitic N and pyrrolic N for the enhanced photocatalytic performance of N-rGO/TiO₂(N₂H₄) photocatalyst (green: pyrrolic N; yellow: graphitic N; pink: pyridinic N): steps (1) and (2) are the rapid transfer of photo-generated electron via the graphitic-N active region, while step (3) is the interfacial oxygen-reduction reaction at the pyrrolic-N active site. (For interpretation of the references to color in the text, the reader is referred to the web version of this article.)

strategy of N-rGO modification for the enhanced photocatalytic activity of TiO₂.

Compared with the pure TiO₂, the enhanced photocatalytic performance of rGO/TiO₂ can be contributed to the rGO nanosheets that function as an excellent electron-cocatalyst owing to its high electron mobility. However, compared with the rGO/TiO₂, the mechanism about the improved photocatalytic activity of N-rGO/TiO₂ is still very unclear. From Table 1, it was found that the main N-bonding configuration in all the N-rGO/TiO₂ samples was the pyrrolic N with an amount of ca. 60–75 wt%. Obviously, after the N element was doped into the rGO nanosheets, one of the important reasons for the higher photocatalytic performance of the N-rGO/TiO₂ can be attributed to the formation of pyrrolic N in rGO nanosheets (see below in Fig. 10b).

For the various N-rGO/TiO₂ samples, their photocatalytic performance can be greatly affected by the different N sources, and it is found that the N-rGO/TiO₂(N₂H₄) shows the highest photocatalytic activity. Therefore, it is very interesting and highly required to further investigate the potential enhanced photocatalytic mechanism of N-rGO/TiO₂(N₂H₄) compared with the N-rGO/TiO₂(NH₃) and N-rGO/TiO₂(CO(NH₂)₂). On the basis of the above results about the XRD, FESEM, TEM, UV–vis, FTIR, and Raman, it was found that the crystal structure, surface morphology, light absorption, and surface microstructures showed no obvious difference for the N-rGO/TiO₂(NH₃), N-rGO/TiO₂(N₂H₄) and N-rGO/TiO₂(CO(NH₂)₂). Therefore, the different photocatalytic performance for the various N-rGO/TiO₂ can only be ascribed to the different N-bonding configurations (XPS results). According to the results of Fig. 3B and Table 1, it is very clear that in addition to the main pyrrolic N, the most obvious difference is that the N-rGO/TiO₂(N₂H₄) photocatalyst shows a higher amount of graphitic N (37%), which is significantly higher than that of N-rGO(NH₃) and N-rGO(CO(NH₂)₂) by a factor of 4.6 and 4.1, respectively. It has been reported that the graphitic N refers to N-atom that substitutes for C atom in the hexagonal ring, and is sp² hybridized with three sp² hybridized C in the N-rGO [30]. Obviously, the graphitic N was formed in the bulk of rGO nanosheets but not at the edges or defects of graphene. Therefore, the basic hexagonal ring structure can be well maintained after the graphitic N doping, which is completely different from the pyrrolic N and pyridinic N. In addition, compared with the C element, the alone electron pairs of nitrogen atoms can form a delocalized conjugated system with the sp²-hybridized carbon frameworks, causing the improvement of the electron-transfer ability. The pyrrolic N is caused by the incorpora-

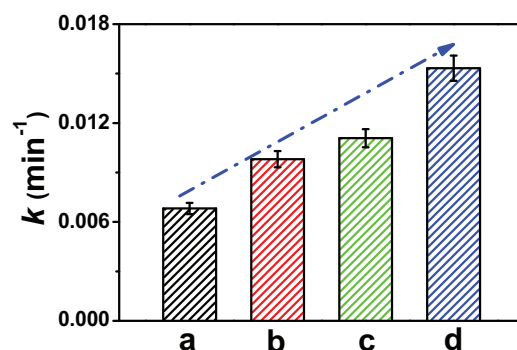


Fig. 9. The further improved photocatalytic performance of N-rGO/TiO₂(N₂H₄) by loading of Cu(II) and Fe(III) electron-cocatalysts on N-rGO surface for the phenol decomposition: (a) TiO₂; (b) N-rGO/TiO₂(N₂H₄); (c) Cu(II)/N-rGO/TiO₂(N₂H₄); and (d) Fe(III)/N-rGO/TiO₂(N₂H₄).

tion of N atoms into a five-member heterocyclic ring, and pyridinic N is from the sp² hybridized N atom with two sp² hybridized C neighbors. Obviously, the pyrrolic N and pyridinic N can only be formed at the edges or defects of graphene, which would produce more defects in the hexagon-ring graphene. It has been reported that the spin density and charge distribution of carbon atoms can be influenced by the neighbor nitrogen dopants, which can induce the formation of “activation region” on the graphene surface [30]. In this study, it is possible that the different “activation region” can be produced by the different N-bonding configuration considering their different formation environment in graphene. It is believed that the graphitic N in the graphene nanosheets can function as the electron-mobility activation region for the rapid and effective transfer of photogenerated electrons from the conduction band of TiO₂, while the pyrrolic N at the edges or defects of graphene can act as the catalytic-reaction activation region for the following oxygen reduction (Fig. 8). To further demonstrate the rapid interfacial electron transfer in N-rGO/TiO₂(N₂H₄), the transient photocurrent responses of various samples are measured and the corresponding results are shown in Figure S3. It was found that compared with the blank TiO₂, the N-doping rGO can significantly improve the photocurrent density of TiO₂, and the N-rGO/TiO₂(N₂H₄) shows the highest photocurrent density, suggesting that the photogenerated electrons can be rapidly captured and transferred from TiO₂ surface via N-rGO/TiO₂(N₂H₄). In addition, based on the calculation of density of state, it is found that the graphitic-N doping can greatly improve its electron density in the conduction band of graphene (Figure S4). Therefore, owing to the synthetic effect of graphitic N (electron-transfer activation region) and pyrrolic N (oxygen-reduction activation site), the prepared N-rGO/TiO₂(N₂H₄) photocatalyst showed the highest photocatalytic performance (Fig. 8).

3.3. The further improved performance of Fe(III)- or Cu(II)/N-rGO/TiO₂

In recent works, the Fe(III) and Cu(II) clusters have been widely demonstrated to be a high-performance electron cocatalyst for rapid oxygen-reduction reaction, which can greatly improve the photocatalytic performance of various photocatalytic materials [46–52]. In this study, the Fe(III) or Cu(II) cocatalyst can be further loaded on the N-rGO nanosheet surface to prepare the Fe(III)/N-rGO/TiO₂ and Cu(II)/N-rGO/TiO₂ photocatalysts by a facile impregnation method [47,50]. It was found that after the addition of Cu(II) and Fe(III) cocatalyst on the N-rGO surface, the photocatalytic performance of the resulting samples can be further improved, as shown in Fig. 9. The enhanced photocatalytic mechanism can also

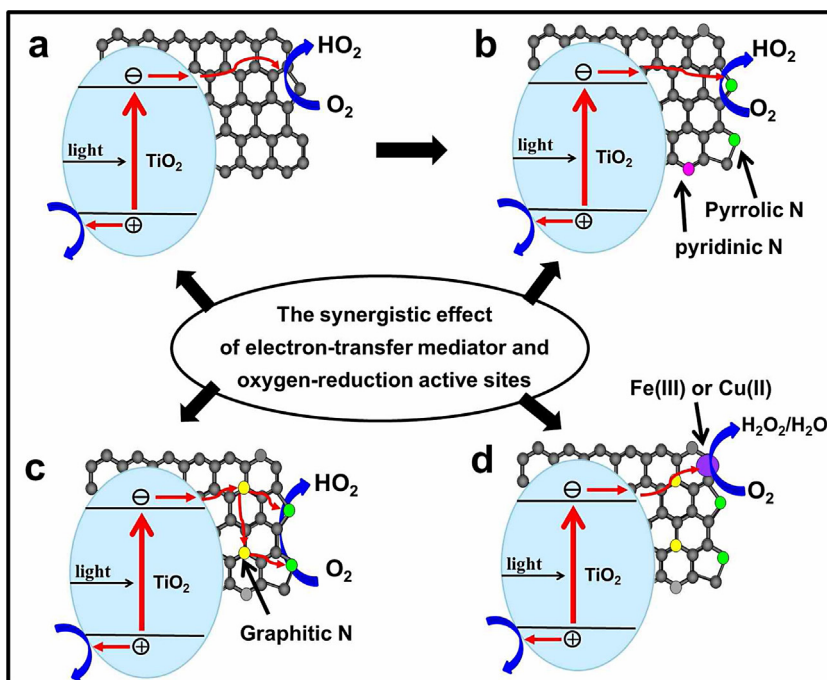


Fig. 10. The compared synergistic effect of graphene-modified TiO_2 photocatalysts: (a) rGO/TiO_2 ; (b) $\text{N-rGO}/\text{TiO}_2(\text{NH}_3)$ or $\text{N-rGO}/\text{TiO}_2(\text{CO}(\text{NH}_2)_2)$; (c) $\text{N-rGO}/\text{TiO}_2(\text{N}_2\text{H}_4)$; and (d) $\text{Cu(II)}/\text{N-rGO}/\text{TiO}_2(\text{N}_2\text{H}_4)$ or $\text{Fe(III)}/\text{N-rGO}/\text{TiO}_2(\text{N}_2\text{H}_4)$.

be well explained by the synthetic effect of electron-transfer mediator and oxygen-reduction active sites, as shown in Fig. 10. For the rGO/TiO_2 composite (Fig. 10a), the rGO nanosheets can rapidly capture the photogenerated electrons, causing the effective separation of the photogenerated electron–hole pairs. In this case, the rGO nanosheets work as the electron-transfer mediator as well as the oxygen-reduction active sites. As for the $\text{N-rGO}/\text{TiO}_2(\text{NH}_3)$ and $\text{N-rGO}/\text{TiO}_2(\text{CO}(\text{NH}_2)_2)$ photocatalysts (Fig. 10b), the pyrrolic N and pyridinic N, which are the main N-binding configuration and only located at the edges of graphene, functions as the oxygen-reduction active sites to improve the interfacial photocatalytic activity. For the $\text{N-rGO}/\text{TiO}_2(\text{N}_2\text{H}_4)$ (Fig. 10c), the high photocatalytic performance can be attributed to the synthetic effect of graphitic N (as electron-transfer activation region) and pyrrolic N (as oxygen-reduction activation site). Considering a further significant improvement of photocatalytic activity of $\text{N-rGO}/\text{TiO}_2(\text{N}_2\text{H}_4)$ by loading Fe(III) and Cu(II) cocatalysts, it is quite believed that the synthetic effect of electron-transfer mediator for graphitic N and oxygen-reduction active sites for Fe(III) or Cu(II) cocatalyst are more effective due to the high-performance oxygen-reduction reaction on the Fe(III) or Cu(II) active sites (Fig. 10d). Therefore, the above results indicated that the synthetic effect of electron-transfer activation region and oxygen reduction activation site is a general and effective strategy for the design of high-performance photocatalytic materials.

4. Conclusions

In summary, the different nitrogen sources (NH_3 , N_2H_4 , and $\text{CO}(\text{NH}_2)_2$) have been used to prepare the $\text{N-rGO}/\text{TiO}_2$ with different N-bonding configurations in graphene. It was found that the $\text{N-rGO}/\text{TiO}_2(\text{NH}_3)$ and $\text{N-rGO}/\text{TiO}_2(\text{CO}(\text{NH}_2)_2)$ photocatalysts mainly showed the pyrrolic N (>70%) and pyridinic N (>10%), while the $\text{N-rGO}/\text{TiO}_2(\text{N}_2\text{H}_4)$ primarily exhibited the pyrrolic N (ca. 63%) and graphitic N (ca. 37%). All the resultant $\text{N-rGO}/\text{TiO}_2$ samples showed a higher photocatalytic performance than the undoped rGO/TiO_2 . Moreover, the $\text{N-rGO}/\text{TiO}_2(\text{N}_2\text{H}_4)$ displayed the highest

photocatalytic activity ($k = 0.29 \text{ min}^{-1}$), which is remarkably larger than that of TiO_2 and rGO/TiO_2 by a factor of 3.63 and 2.64, respectively. On the basis of the above results, a synergistic effect of graphitic N and pyrrolic N in graphene is proposed to account for the enhanced photocatalytic performance of $\text{N-rGO}/\text{TiO}_2(\text{N}_2\text{H}_4)$, namely, the graphitic-N doped graphene serves as an effective electron mediator for the photogenerated electrons while the pyrrolic-N doped graphene functions as the oxygen-reduction active site to rapidly promote the following interfacial catalytic reaction. The present report can provide some new insights for the ingenious synthesis of highly effective photocatalytic materials.

Acknowledgements

This work was supported by the National Natural Science Foundation of China (51472192, 21477094, and 21277107) and 973 Program (2013CB632402). This work was also financially supported by program for new century excellent talents in university (NCET-13-0944), Wuhan Youth Chenguang Program of Science and Technology (2014070404010207), and the Fundamental Research Funds for the Central Universities (WUT 2015IB002).

Appendix A. Supplementary data

Supplementary data associated with this article can be found, in the online version, at <http://dx.doi.org/10.1016/j.apcatb.2015.08.049>.

References

- [1] S.G. Kumar, L.G. Devi, *J. Phys. Chem. A* 115 (2011) 13211–13241.
- [2] H. Tada, T. Kiyonaga, S. Naya, *Chem. Soc. Rev.* 38 (2009) 1849–1858.
- [3] H.F. Cheng, K. Fukui, Y. Kuwahara, K. Mori, H. Yamashita, *J. Mater. Chem. A* 3 (2015) 5244–5258.
- [4] R. Asahi, T. Morikawa, T. Ohwaki, K. Aoki, Y. Taga, *Science* 293 (2001) 269–271.
- [5] K. Mori, M. Kawashima, H. Yamashita, *Chem. Commun.* 50 (2014) 14501–14503.
- [6] Y.P. Yuan, L.S. Yin, S.W. Cao, G.S. Xu, C.H. Li, C. Xue, *Appl. Catal. B-Environ.* 168 (2015) 572–576.

- [7] P. Wang, J. Wang, T. Ming, X. Wang, H. Yu, J. Yu, Y. Wang, M. Lei, *ACS Appl. Mater. Interfaces* 5 (2013) 2924–2929.
- [8] L.F. Qi, J.G. Yu, M. Jaroniec, *Phys. Chem. Chem. Phys.* 13 (2011) 8915–8923.
- [9] X. Wang, S. Zhan, Y. Wang, P. Wang, H. Yu, J. Yu, C. Hu, *J. Colloid Interface Sci.* 422 (2014) 30–37.
- [10] H.G. Yu, R. Liu, X.F. Wang, P. Wang, J.G. Yu, *Appl. Catal. B-Environ.* 111 (2012) 326–333.
- [11] P. Wang, Y. Xia, P. Wu, X. Wang, H. Yu, J. Yu, *J. Phys. Chem. C* 118 (2014) 8891–8898.
- [12] Y. Gu, M. Xing, J. Zhang, *Appl. Surf. Sci.* 319 (2014) 8–15.
- [13] M. Aleksandrak, P. Adamski, W. Kukulka, B. Zielinska, E. Mijowska, *Appl. Surf. Sci.* 331 (2015) 193–199.
- [14] Z.W. Seh, S. Liu, M. Low, S.-Y. Zhang, Z. Liu, A. Mlayah, M.-Y. Han, *Adv. Mater.* 24 (2012) 2310–2314.
- [15] Z. Zheng, B. Huang, X. Qin, X. Zhang, Y. Dai, M.-H. Whangbo, *J. Mater. Chem.* 21 (2011) 9079–9087.
- [16] M. Xu, T. Liang, M. Shi, H. Chen, *Chem. Rev.* 113 (2013) 3766–3798.
- [17] Y. Zhu, D.K. James, J.M. Tour, *Adv. Mater.* 24 (2012) 4924–4955.
- [18] L. Dai, *Acc. Chem. Res.* 46 (2013) 31–42.
- [19] Q.J. Xiang, J.G. Yu, M. Jaroniec, *Chem. Soc. Rev.* 41 (2012) 782–796.
- [20] B.F. Machado, P. Serp, *Catal. Sci. Technol.* 2 (2012) 54–75.
- [21] Q. Xiang, J. Yu, *J. Phys. Chem. Lett.* 4 (2013) 753–759.
- [22] M.Q. Yang, Y.-J. Xu, *Phys. Chem. Chem. Phys.* 15 (2013) 19102–19118.
- [23] C. Hua, F. Chen, T. Lu, C. Lian, S. Zheng, Q. Hu, S. Duo, R. Zhang, *Appl. Surf. Sci.* 317 (2014) 648–656.
- [24] F. Zhao, B. Dong, R. Gao, G. Su, W. Liu, L. Shi, C. Xia, L. Cao, *Appl. Surf. Sci.* 351 (2015) 303–308.
- [25] Q.J. Xiang, B. Cheng, J.G. Yu, *Angew. Chem. Int. Ed.* (2015), <http://dx.doi.org/10.1002/anie.201411096>.
- [26] P. Wang, J. Wang, X.F. Wang, H.G. Yu, J.G. Yu, M. Lei, Y.G. Wang, *Appl. Catal. B-Environ.* 132 (2013) 452–459.
- [27] P. Wang, J. Wang, T.S. Ming, X.F. Wang, H.G. Yu, J.G. Yu, Y.G. Wang, M. Lei, *ACS Appl. Mater. Interfaces* 5 (2013) 2924–2929.
- [28] G.Q. Luo, X.J. Jiang, M.J. Li, Q. Shen, L.M. Zhang, H.G. Yu, *ACS Appl. Mater. Interfaces* 5 (2013) 2161–2168.
- [29] P. Wang, T. Ming, G. Wang, X. Wang, H. Yu, J. Yu, *J. Mol. Catal. A-Chem.* 381 (2014) 114–119.
- [30] H.B. Wang, T. Maiyalagan, X. Wang, *ACS Catal.* 2 (2012) 781–794.
- [31] Z. Mou, Y. Wu, J. Sun, P. Yang, Y. Du, C. Lu, *ACS Appl. Mater. Interfaces* 6 (2014) 13798–13806.
- [32] M.S.A.S. Shah, W.-J. Kim, J. Park, D.K. Rhee, I.-H. Jang, N.-G. Park, J.Y. Lee, P.J. Yoo, *ACS Appl. Mater. Interfaces* 6 (2014) 20819–20827.
- [33] C. Lavorato, A. Primo, R. Molinari, H. Garcia, *Chem. Eur. J.* 20 (2014) 187–194.
- [34] F. Pei, S. Xu, W. Zuo, Z. Zhang, Y. Liu, S. Cao, *Int. J. Hydrogen Energy* 39 (2014) 6845–6852.
- [35] C. Dong, K.-L. Wu, X.-W. Wei, J. Wang, L. Liu, B.-B. Jiang, *Appl. Catal. A: Gen.* 488 (2014) 11–18.
- [36] F. Meng, J. Li, S.K. Cushing, M. Zhi, N. Wu, *J. Am. Chem. Soc.* 135 (2013) 10286–10289.
- [37] P. Chen, T.-Y. Xiao, H.-H. Li, J.-J. Yang, Z. Wang, H.-B. Yao, S.-H. Yu, *ACS Nano* 6 (2012) 712–719.
- [38] L. Jia, D.-H. Wang, Y.-X. Huang, A.-W. Xu, H.-Q. Yu, *J. Phys. Chem. C* 115 (2011) 11466–11473.
- [39] H. Yu, G. Cao, F. Chen, X. Wang, J. Yu, M. Lei, *Appl. Catal. B-Environ.* 160 (2014) 658–665.
- [40] M.S.A. Sher Shah, A.R. Park, K. Zhang, J.H. Park, P.J. Yoo, *ACS Appl. Mater. Interfaces* 4 (2012) 3893–3901.
- [41] S.D. Perera, R.G. Mariano, K. Vu, N. Nour, O. Seitz, Y. Chabal, K.J. Balkus, *ACS Catal.* 2 (2012) 949–956.
- [42] J. Li, X. Li, P. Zhao, D.Y. Lei, W. Li, J. Bai, Z. Ren, X. Xu, *Carbon* 84 (2015) 460–468.
- [43] Q.J. Xiang, J.G. Yu, M. Jaroniec, *J. Am. Chem. Soc.* 134 (2012) 6575–6578.
- [44] H.L. Wang, J.T. Robinson, X.L. Li, H.J. Dai, *J. Am. Chem. Soc.* 131 (2009) 9910–9911.
- [45] D.C. Luo, G.X. Zhang, J.F. Liu, X.M. Sun, *J. Phys. Chem. C* 115 (2011) 11327–11335.
- [46] H. Irie, S. Miura, K. Kamiya, K. Hashimoto, *Chem. Phys. Lett.* 457 (2008) 202–205.
- [47] H. Yu, H. Irie, Y. Shimodaira, Y. Hosogi, Y. Kuroda, M. Miyauchi, K. Hashimoto, *J. Phys. Chem. C* 114 (2010) 16481–16487.
- [48] H. Yu, L. Xu, P. Wang, X. Wang, J. Yu, *Appl. Catal. B-Environ.* 144 (2014) 75–82.
- [49] X. Wang, K. Wang, K. Feng, F. Chen, H. Yu, J. Yu, *J. Mol. Catal. A-Chem.* 391 (2014) 92–98.
- [50] H. Yu, H. Irie, K. Hashimoto, *J. Am. Chem. Soc.* 132 (2010) 6898–6899.
- [51] C. Huang, J. Hu, S. Cong, Z. Zhao, X. Qiu, *Appl. Catal. B-Environ.* 174 (2015) 105–112.
- [52] G. Yin, M. Nishikawa, Y. Nosaka, N. Srinivasan, D. Atarashi, E. Sakai, M. Miyauchi, *ACS Nano* 9 (2015) 2111–2119.